scientific reports

Check for updates

OPEN

Displacement and stress response of open-web girders under near field explosive loading

Zongyuan Fan[1,2], Kaicong Kuang[1,4], Yanhui Wei[1,2✉], Jing Chen[1,2], Penggang Tian[3], Bingzhen Zhao[3] & Kejian Ma[1,2]

This study employed numerical simulation to investigate the dynamic response characteristics of open-web girders subjected to proximity blast loading and to compare these characteristics with those of solid-web girders. The research utilized the Coupled Eulerian–Lagrangian (CEL) method for simulation, effectively combining the advantages of both Eulerian and Lagrangian approaches. This method mitigated issues related to mesh distortion while accurately modeling the damage inflicted by blast loads on the structures. The primary objective of this study was to elucidate the response differences between open-web and solid-web girders under blast loading, thereby providing a reference for relevant engineering design. Researchers used Abaqus finite element software to create three-dimensional solid models of both structural types and conducted numerical simulations to achieve these objectives. Results indicated that, although open-web girders and solid-web girders exhibited similar dynamic responses under blast loading, the nodes of open-web girders were more vulnerable to damage. Further analysis revealed that the local moments at the top rib, bottom rib, and shear key of open-web girders were critical to the overall displacement response, particularly when the shear key width was narrow. Increasing the shear key width could align the reaction of open-web girders more closely with that of solid-web girders. Significant differences were observed in reinforcement stresses between open-web and solid-web girders with identical longitudinal reinforcement configurations. These findings can enhance the understanding of the response behavior of open-web girders under blast loading and provide valuable insights for engineering designs.

Keywords Open-web girder, Numerical simulation, Blast loading, CEL method, Response

After more than 30 years of continuous development, open-web sandwich plates, as shown in Fig. 1, have become widely used in practical engineering and have yielded significant economic benefits[1,2]. Due to their excellent three-dimensional mechanical properties, they are highly favored for long-span structures. In recent years, several researchers have conducted extensive studies on the static and dynamic characteristics of open-web sandwich plates and their components. For instance, Dingyuan Liu et al.[3] proposed the quasi-sandwich plate variational method of open-web sandwich plates bending theory based on the variational method. Fang Yu et al.[4] conducted a comprehensive experimental study on an open-web sandwich plate bridge to verify its static load-carrying capacity. Kejian Ma et al.[5] investigated the application of reinforced concrete open-web sandwich plates and determined an economically reasonable span. Additionally, Lan Jiang et al.[6] analyzed the acceleration factors that affect the steel–concrete composite open-web sandwich plate and conducted experiments to verify certain parameters. Duodong Wu et al.[7] employed numerical simulation methods to analyze the natural vibration characteristics of an open-web sandwich plate floor structure and the vibration acceleration response of the floor structure under various loads. Tong Xiao et al.[8] utilized MIDAS/Gen finite element software to investigate the structural dynamic characteristics and seismic performance of a steel–concrete composite space grid box structure, comparing it with the traditional frame structure.

With the widespread application of open-web sandwich plates in large-span public buildings and industrial factories, researchers have primarily focused on conducting in-depth research on the response of open-web sandwich plates under static and dynamic loads. However, there has been limited attention given to the dynamic response and associated damage of open-web sandwich plates under explosive loads. In recent years, there have

[1]Research Center of Space Structures, Guizhou University, Guiyang 550025, China. [2]Key Laboratory of Structural Engineering of Guizhou Province, Guiyang 550025, China. [3]Future City Innovation Technology Co., Ltd, Shaanxi Construction Engineering Holding Group, Xian 710000, China. [4]College of Civil Engineering Guizhou University, Guiyang 550025, China. ✉email: yhwei@gzu.edu.cn
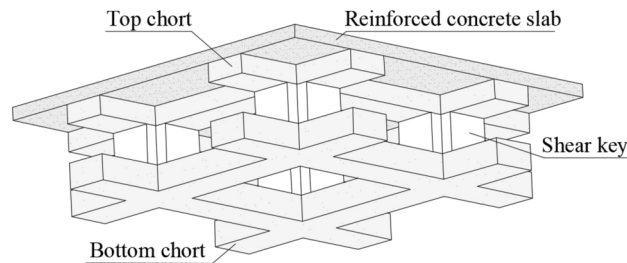
Fig. 1. Axonometric drawing of the open-web sandwich plate.

been several explosion accidents reported worldwide. For instance, on October 24, 2021, an explosion accident occurred in the Materials Laboratory of the School of Materials Science and Technology at Nanjing University of Aeronautics and Astronautics. Similarly, on May 24, 2022, a residential building in Wujin District, Changzhou City, exploded due to a leak of bottled liquefied gas, resulting in the collapse of the building. Additionally, on July 19, 2022, a gas explosion occurred in a residential building in Beichen District, Tianjin. Another example is the store explosion in Gaomi City, Weifang, Shandong, on August 13, 2023, where natural gas was the cause. These explosion accidents not only resulted in casualties but also caused significant damage to the building structures. Considering that the open-web sandwich plate structure may be exposed to potential risks of explosion hazards such as canned gas, dust, and natural gas, it is imperative to conduct comprehensive research on the anti-explosion performance of the open-web sandwich plate structure and its components. The open-web girder[9], as the primary load-bearing element of the open-web sandwich plate, plays a vital role. Therefore, it is crucial to investigate the dynamic response of open-web girders under explosive loads. This analysis will contribute to a better understanding of the anti-explosion performance of open-web sandwich plates and can offer valuable insights for future research on enhancing their anti-explosion capabilities.

The explosion is a highly complex physical and chemical process, and finding a simple and effective formula to accurately describe the damage caused by explosion loads to structures has not yet been achieved[10]. Additionally, conducting large-scale explosion tests is challenging due to the harsh experimental conditions. However, in recent years, the advancement of finite element software and computer computing capabilities has enabled researchers to increasingly utilize numerical simulation methods for simulating the intricate process of explosion tests. For example, Yanchao Shi et al.[11] utilized finite element analysis to investigate the progressive collapse process of reinforced concrete frames subjected to explosive loads with non-zero initial conditions. Jing Wang et al.[12] conducted local failure tests on concrete slabs under close-range explosion loads and thoroughly examined the failure patterns of reinforced concrete slabs in such scenarios, and numerical simulation analysis was performed using the finite element software ANSYS/LS-DYNA. Jun Li et al.[13] conducted a comparative study on ultra-high performance concrete slabs and ordinary strength concrete slabs under contact explosion and carried out numerical simulation analysis of the experiment using finite element software ANSYS/LS-DYNA. Vaishnavi et al.[14] employed numerical simulation to analyze the detonation pressure waves generated under explosive loads and further developed the floor pressure pulse curve using MATLAB software. Bo Yan et al.[15] utilized the ANSYS/LS-DYNA software to examine the damage modes of reinforced concrete components when subjected to close-range explosion loads and compared them with experimental data. D. Rajkumar et al.[16] employed the finite element software ANSYS/LS-DYNA to simulate the response of reinforced concrete columns under various explosive load parameters. Similarly, Sherong Zhang et al.[17] utilized numerical analysis to simulate the failure mode of concrete gravity dams under explosive loads. Additionally, Chahmi Oucif et al.[18] conducted detailed numerical simulations to study the process of high-speed impact penetrating reinforced concrete panels. Finally, Jie Luo et al.[19] employed numerical simulation methods to analyze the dynamic response of steel open-web sandwich plates and extensively investigated the corresponding stress transfer modes. Given the extensive range and significance of open-web sandwich plate structures in practical engineering applications, particularly their complex behavior under explosive loads, a comprehensive study of their dynamic response characteristics is essential. This research will focus on the open-web girder, a critical component of the open-web sandwich plate, and aims to investigate the dynamic response of the structure subjected to blast loads through numerical simulation methods. Specifically, the CEL finite element method will be employed, as it effectively simulates the large deformations induced by blast loads while mitigating issues related to mesh distortion. By comparing the displacement and stress responses of the open-web girder to those of the solid-web girder under explosive loading, this study will enhance our understanding of the open-web girder's response behavior in such conditions. Furthermore, it will provide valuable insights for engineering design and establish a theoretical foundation for implementing effective explosion prevention measures, thereby significantly contributing to enhancing structural safety in extreme environments.

Description of the coupled method

Various methods are available for simulating the dynamic response of structures under explosive loads, including the CEL method, SPH method, and FEM-SPH method[20,21]. In this study, the CEL finite element method is selected. The CEL method is a coupled finite element algorithm that combines the Euler finite element method with the Lagrangian finite element method. By utilizing the Euler region, we can analyze the large deformation flow problem that occurs after an explosive explosion and prevent grid distortion. On the other hand, the

Lagrangian method is employed to calculate the deformation of spatial grid box structures. The coupling between the Euler and Lagrangian regions is achieved through penalty functions. This method proves to be effective in accurately simulating the significant damage caused to structures by explosive loads.

Material model
Material model for concrete

The selection of an appropriate constitutive model is crucial for accurate numerical simulation results, due to significant differences in the mechanical properties of materials under high strain rates compared to static loads[22,23]. In this study, the material constitutive model of JH-2[18,24] is used to describe the constitutive relationship of concrete. The model comprises three parts: strength model, damage model, and state equation, which can effectively describe the failure process of materials caused by large deformation, high strain rate, and high pressure.

Strength model
According to the damage factor D, the strength model can be divided into three states: intact state, damage state, or fracture state. According to Fig. 2a, these are expressed as the normalized equivalent stress versus normalized hydrostatic pressure.

a. intact state: $D = 0$

$$\sigma_i^* = A(P^* + T^*)^N (1 + Cln\dot{\varepsilon}^*) \leq \sigma_i^{max} \tag{1}$$

b. damage state: $0 < D < 1$

$$\sigma^* = \sigma_i^* - D(\sigma_i^* - \sigma_f^*) \tag{2}$$

c. fracture state: $D = 1$

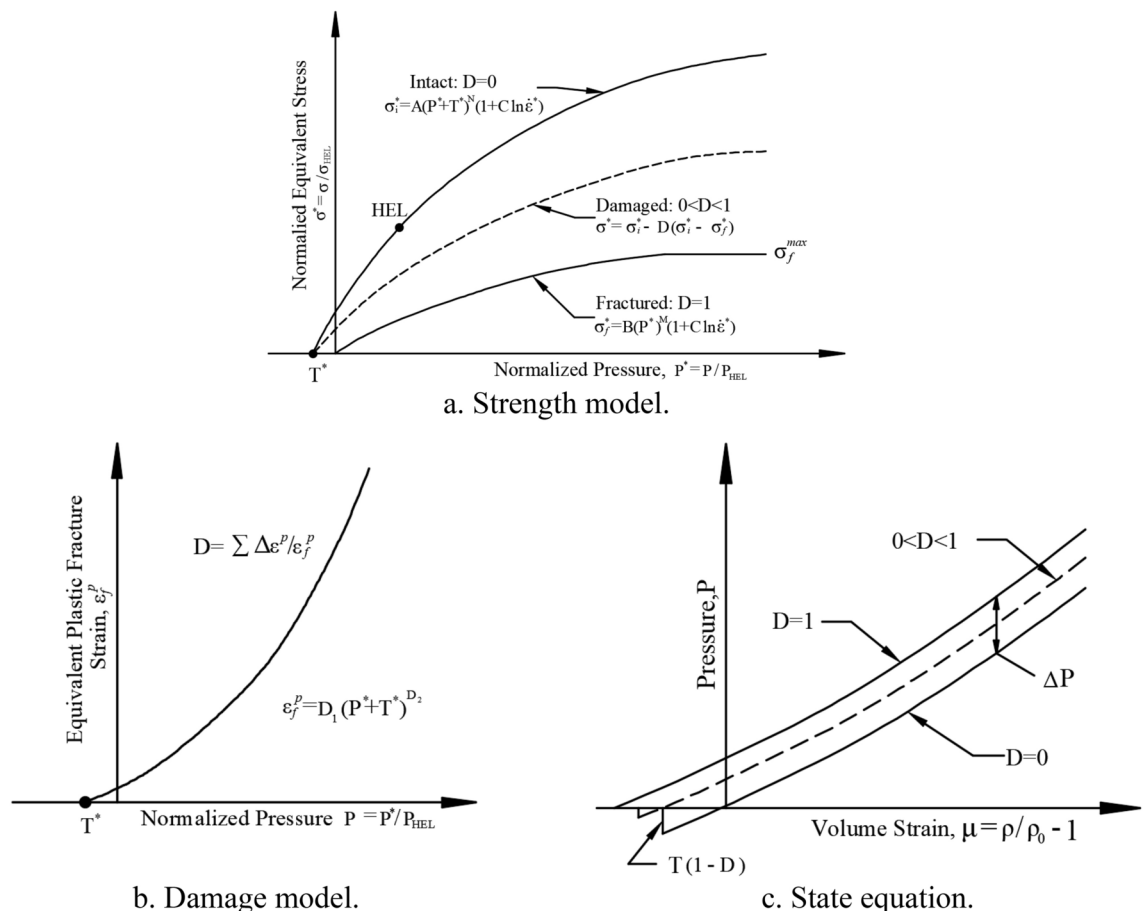$$\sigma_f^* = B(P^*)^M (1 + Cln\dot{\varepsilon}^*) \leq \sigma_f^{max} \tag{3}$$

Fig. 2. JH-2 model[18,24]. (**a**). Strength model. (**b**). Damage model. (**c**). State equation.

$\rho(\text{kg/m}^3)$	G(GPa)	A	B	C	N	m	$\dot{\varepsilon}_0$	T(MPa)
2400	12.5	0.6304	0.2101	0.006	0.8437	0.8437	1	3.4
D_1	D_2	HEL(GPa)	P_{HEL}(GPa)	K_1(GPa)	K_2(GPa)	K_3(GPa)		
0.6	0.1	1.481	0.811	16.667	73.19	-236.2		

Table 1. C30 concrete JH-2 constitutive parameters.

σ_i^{max}	σ_f^{max}	β	$\overline{\epsilon}^{\text{pl}}_{\text{f, max}}$	$\overline{\epsilon}^{\text{pl}}_{\text{f, min}}$	F_S	IDamage
1.2	0.26	1	1	0.001	0.75	0

Table 2. Jh-2 constitutive control parameters.

where σ is the actual Von-Mises equivalent stress, σ^* is the normalized equivalent stress, σ_i^* is the normalized intact equivalent stress, σ_f^* is the normalized fractured equivalent stress, σ_{HEL} is the equivalent stress at the Hugoniot elastic limit (HEL), P^* is the normalized pressure, P is the actual pressure, P_{HEL} is the pressure at the HEL, T^* is the normalized maximum tensile hydrostatic pressure, T is the maximum tensile pressure that the material can withstand, $\dot{\varepsilon}^*$ is the dimensionless strain rate has the general form $\dot{\varepsilon}^* = \varepsilon/\varepsilon_0$, ε is the actual strain rate, ε_0 is the reference strain rate(ε_0=1.0 s^{-1}), σ_i^{max} and σ_f^{max} are the optional limits for the strengths and A , B, C, M, and N are the material parameters.

Damage model
As is shown in Fig. 2b, the cumulative calculation formula for fracture damage is:

$$D = \sum \Delta\varepsilon^p / \varepsilon_f^p \tag{4}$$

$$\varepsilon_f^p = D_1(P^* + T^*)^{D_2} \tag{5}$$

where $\Delta\varepsilon^p$ is the increment in equivalent plastic strain, ε_f^p is the equivalent plastic strain to fracture under constant pressure, D_1 and D_2 are material parameters.

State equation
The equation of state is used to describe the relationship between the hydrostatic pressure and volumetric strain of materials, as shown in Fig. 2c.
a. When the material is undamaged (D=0), the equation of state can be expressed as:

$$P = K_1\mu + K_2\mu^2 + K_3\mu^3 \text{If } \mu > 0 \tag{6}$$

$$P = K_1\mu \text{If } \mu < 0 \tag{7}$$

b. After the accumulation of damage begins (D>0), an additional pressure term ΔP is added, and the equation is expressed as:

$$P = K_1\mu + K_2\mu^2 + K_3\mu^3 + \Delta P \tag{8}$$

The pressure increment is determined from energy considerations as

$$\Delta P_{t+\Delta t} = -K_1 \cdot \mu_{t+\Delta t} + \sqrt{(K_1 \cdot \mu_{t+\Delta t} + \Delta P_t)^2 + 2 \cdot \beta \cdot K_1 \cdot \Delta U} \tag{9}$$

where β is the fraction of the elastic energy loss converted to potential hydrostatic energy ($0 < \beta < 1$).

The constitutive parameters of the concrete In this study are calculated using the values fitted in the literature[25], as shown in Table 1. The control parameters not provided in the literature were calibrated using numerical simulation methods to reproduce the existing explosion tests in the literature[26], as shown in Table 2.

Material model for steel
In explosion and impact research, the Johnson–Cook constitutive model[27] is commonly used to describe materials subjected to high pressures and strain rates. The yield stress is expressed as Eq. 10. This article adopts

$\rho(\mathrm{kg/m^3})$	$E(\mathrm{GPa})$	v	$A(\mathrm{MPa})$	$B(\mathrm{MPa})$	n	m	C	$\dot{\varepsilon}_0$
7830	209.48	0.28	420	510	0.26	1.03	0.014	1

Table 3. Constitutive parameters of steel bars I[26].

$\rho(\mathrm{kg/m^3})$	$E(\mathrm{GPa})$	v	$A(\mathrm{MPa})$	$B(\mathrm{MPa})$	n	m	C	$\dot{\varepsilon}_0$
7830	209	0.28	267.4	365	0.6413	1.762	0.0545	0.0001

Table 4. Constitutive parameters of steel bars II[28].

$\rho_0(\mathrm{kg/m^3})$	$A(\mathrm{GPa})$	$B(\mathrm{GPa})$	ω	R_1	R_2	$E_m(\mathrm{J/kg})$	Detonation wave speed (m/s)
1630	373.8	3.347	792	510	0.014	3,680,000	6930

Table 5. Constitutive parameters of TNT[30].

$\rho_0(\mathrm{kg/m^3})$	R(J/kg·K)	p_A (N/m²)	Specific heat(J/kg·K)	Viscosity(N·s·m⁻²)
1.293	287	101,325	717.5	1.7894×10^{-5} (at 288 K)

Table 6. Constitutive parameters of Air[30].

two types of steel bars, with yield strengths of 420 MPa and 267 MPa, respectively. The specific parameters are shown in Tables 3, 4.

$$\bar{\sigma} = \left[A + B\left(\bar{\varepsilon}^{pl}\right)^n \right] \left[1 + C ln \left(\frac{\dot{\varepsilon}^{pl}}{\dot{\varepsilon}_0} \right) \right] (1 - \widehat{\theta}^m) \tag{10}$$

where $\bar{\varepsilon}^{pl}$ is the effective plastic strain, $\dot{\varepsilon}^{pl}$ is the equivalent plastic strain rate, $\widehat{\theta}^m$ is the nondimensional temperature, A is the initial yield stress, B is the hardening constant, C is the strain rate constant and $\dot{\varepsilon}_0$ are material parameters measured, n is the hardening exponent and m is the thermal softening exponent.

Material model for explosive

To model the explosive (TNT), the Jones-Wilkins-Lee (JWL) equation of state[29] is used. This equation reproduces the phenomenon of gas expansion following detonation:

$$P = A \left(1 - \frac{\omega\rho}{R_1\rho_0} \right) e^{-R_1 \frac{\rho}{\rho_0}} + B \left(1 - \frac{\omega\rho}{R_2\rho_0} e^{-R_1 \frac{\rho}{\rho_0}} \right) + \omega E_m \rho \tag{11}$$

where P is the detonation pressure, ρ_0 is the explosive density, ρ is the density of detonation products, A, B, R_1, R_2, ω are the Fixed parameters for explosives and E_m is the Initial internal energy per unit volume. The specific parameters are shown in Table 5.

Material model for air

Using the EOS[31] for the ideal gas, we can write the equation of state for a gas as follows:

$$p + p_A = \rho R(\theta - \theta^z) \tag{12}$$

This equation consists of p_A being the ambient pressure, R being the gas constant, θ being the current temperature, and θ^z being the absolute zero. The specific parameters are shown in Table 6.

Validation of the validity of the parameter

Using numerical analysis to simulate the experiments in Ref.[26] and compare the test results, this study verifies the validity of the test methods and parameters. Comparing and analyzing the displacement and damage of a concrete beam under the explosive load of 8 kg (TNT) with 0.6 m spacing, the scaled distance was 0.3 m/kg$^{1/3}$.
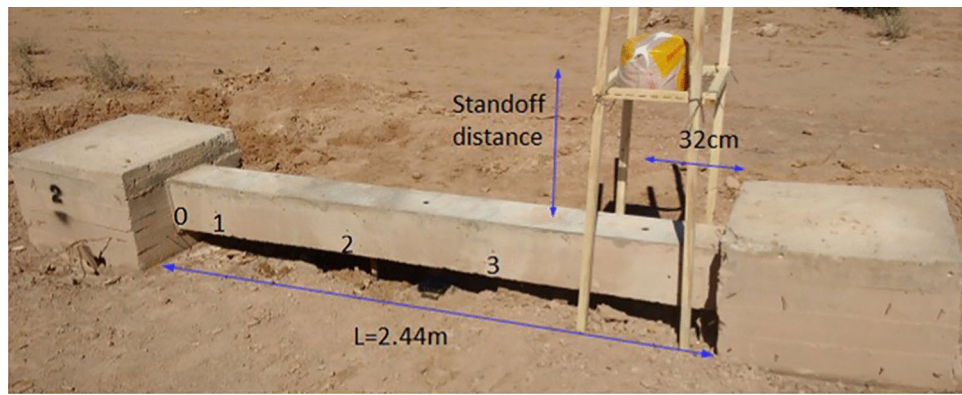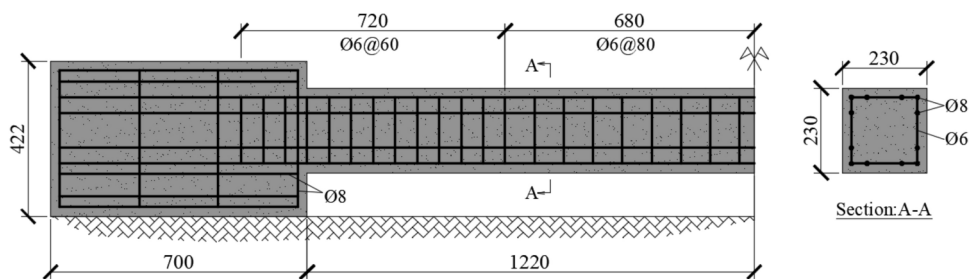
Fig. 3. Experimental setup.

Fig. 4. Member geometry and reinforcement characteristics.

Figures 3, 4 show that the dimensions of the concrete slab match those described in the literature. Concrete is graded as C30, while steel bars are graded as 420 MPa. The constitutive laws and parameters of concrete, steel bars, explosives, and air have been explained above.

This study employed ABAQUS finite element software for modeling, utilizing the explicit dynamics algorithm to address a transient nonlinear dynamics problem, specifically explosion loading. Concrete elements were modeled using solid units, whereas steel bars were represented by beam units. The Euler region incorporated two distinct materials: air and explosives. The explosives were configured as a cylindrical object, with the initiation center positioned at the geometric center of the explosive surface. The distance from the explosive's center point to the reinforced concrete beam was 0.6 m. To account for the influence of material mesh, the concrete and steel mesh sizes were both set to 10 mm, while the mesh size in the Euler region was established at 15 mm. The concrete and steel bars were interconnected using the embedded region method. For the interaction between the blast wave and the structure, both normal and tangential contact types were configured. Fixed constraints were applied at the bottom of both ends of the concrete beam. Furthermore, the simulation results also considered the effects of ground reflection.

By comparing and analyzing the numerical simulation results shown in Fig. 5 with the experimental results, it can be observed that there is good consistency in the location of structural damage and the depth of external erosion. Additionally, the overall bending deformation of the beam exhibits a similar trend. The vertical displacement of the structure, as depicted in Fig. 6, demonstrates that the numerical simulation results align with the overall trend of the experimental results. Specifically, at position 872 mm, the vertical displacement of the experimental and numerical simulation results is 21 and 28.2 mm, respectively. The difference between the two is 7.25 mm, resulting in a relative error of 34.5%. At position 1540 mm, the vertical displacements of the experimental and numerical simulation results were 67.3 and 71.9 mm, respectively, with a relative error of only 4.6 mm and an error of just 6.8%. Therefore, it can be concluded that the methods and parameters employed have demonstrated their effectiveness in numerical simulation, allowing for the accurate reproduction of the experimental results.

Structural dynamic response analysis
### Description of the analysis model

The study focuses on the open-web girder structure and compares the displacement and stress responses of three different structural models: open-web girder I, open-web girder II, and Equivalent beam (solid-web girder) under explosive loads. The specific structural parameters are depicted in Figs. 7, 8. The dimensions of the top ribs, bottom ribs, and shear keys of the open-web girder are determined according to the technical specification[9], while the dimensions of the Equivalent beam are based on the open-web girder. The open-web girder II model is based on the open-web girder I by adding a 300 mm wide shear key, aiming to study the effect of increasing the

Results of the experiment.
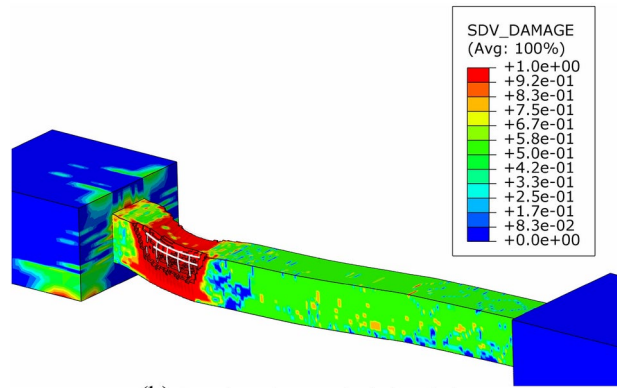
(b) Results of numerical simulation.

Fig. 5. Damage results of concrete. (**a**) Results of the experiment. (**b**) Results of numerical simulation.
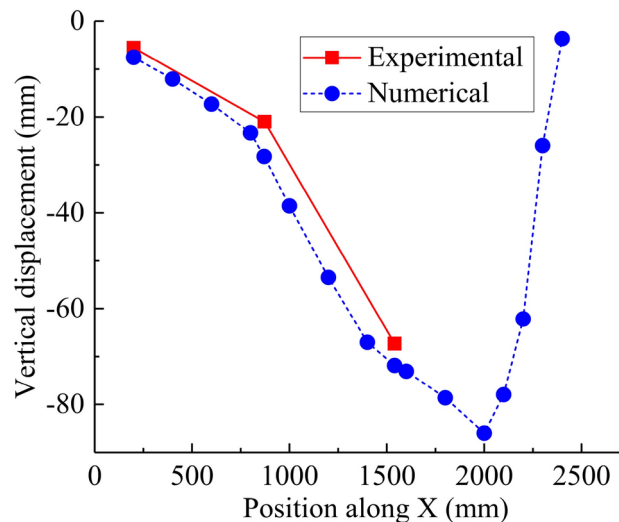
Fig. 6. Vertical displacement results of beam.

shear key width on structural response. The size of the Equivalent beam is determined based on the equivalent calculation size[9] of open-web girder I and both have the same cross-sectional moment of inertia to analyze the influence of equivalent calculation on the structural stress characteristics.

To ensure uniform explosive pressure and load on three types of structures, a layer of reinforced concrete slabs with equal quantity and strength is installed on the upper part of the three structures and uses the same number and strength of longitudinal steel bars, as well as stirrups with the same strength and spacing, while the remaining steel reinforcement is configured according to the structural requirements. The concrete strength used in this study is C30, the yield strength of longitudinal steel bars is 420 MPa, and the yield strength of all steel bars in reinforced concrete slabs and stirrups is 267 MPa. The explosive load chosen is a 20 kg cubic explosive, positioned 0.8 m above the structure and 3.175 m from the end of the structure. The equivalent distance is calculated as 0.295 m/kg$^{1/3}$.

The constitutive model parameters of this material were selected based on the data provided in Chapter 3. To eliminate errors caused by grid effects, we used the same type of units and grid size for all three models.
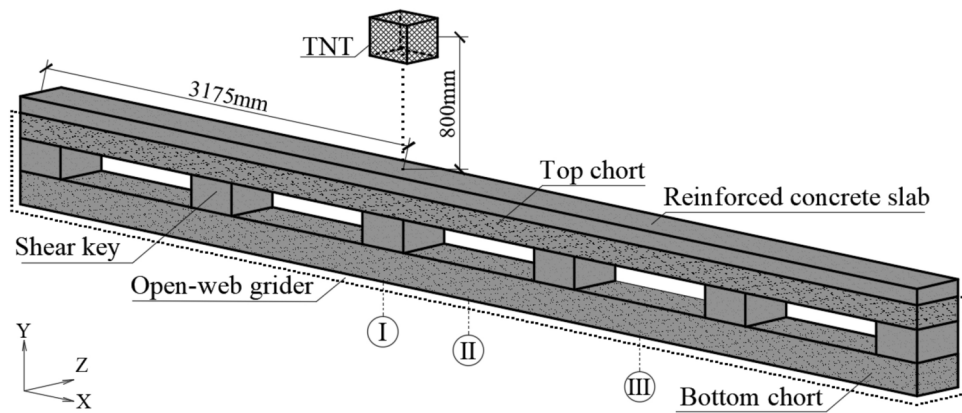
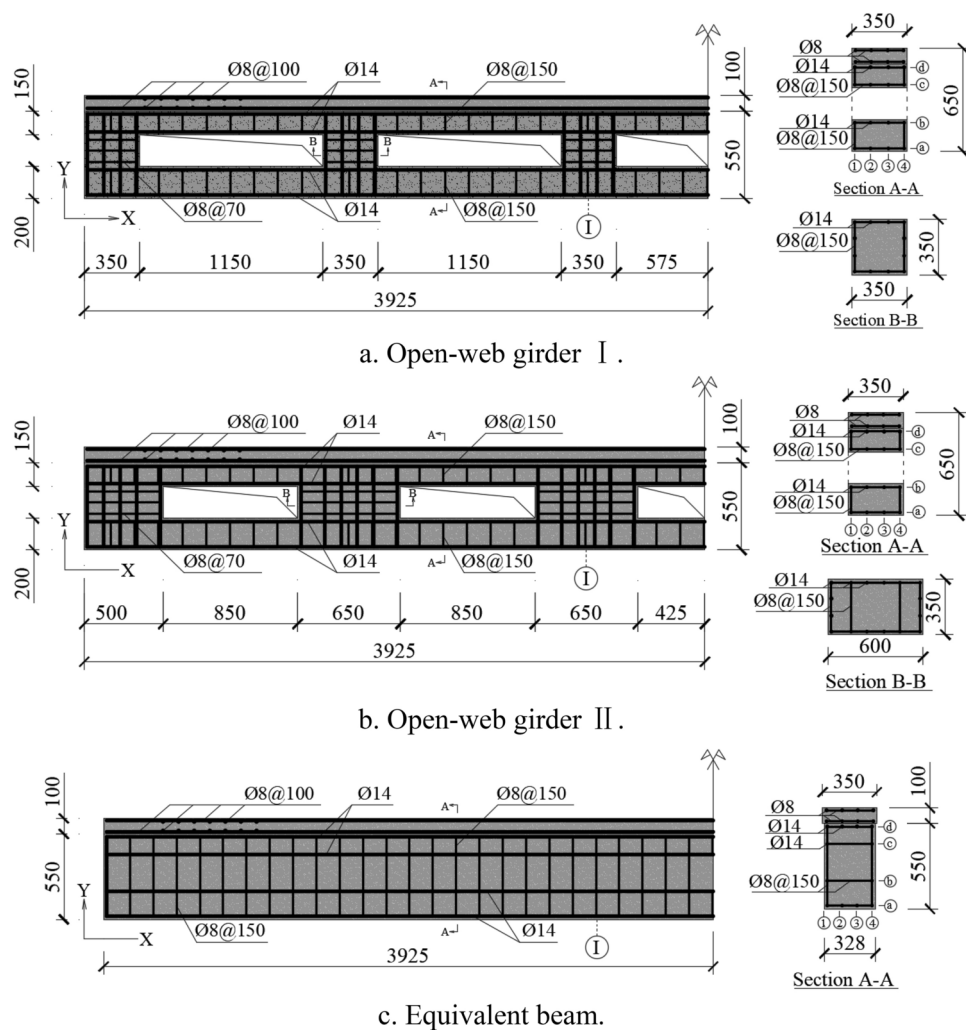**Fig. 7**. Spatial schematic diagram of open-web girder I.

Fig. 8. Member geometry and reinforcement characteristics. (**a**) Open-web girder I. (**b**) Open-web girder II. (**c**) Equivalent beam.

Specifically, solid elements with a mesh size of 15 mm were used for concrete, while beam elements with a grid size of 25 mm were used for reinforcement. In the numerical simulation process, we took into account the influence of air viscosity. Therefore, we specify two materials, explosive and air, in the Euler region, using a 20 mm grid size for this region.

Damage analysis

Figure 9 illustrates the concrete damage cloud maps for three different types of structures. The primary areas of damage for the three structures are concentrated on the concrete slab nearest to the center of the explosion. The severely damaged areas share similar appearances and sizes, and none of the three structures have completely lost their load-bearing capacity. In terms of surface damage, open-web girder I exhibits slightly more severe damage compared to the other two structures. Specifically, there are varying degrees of damage observed at the connection points of the top ribs, bottom ribs, and shear keys of both open-web girder I and open-web girder

a. Open-web girder Ⅰ.

b. Open-web girder Ⅱ.
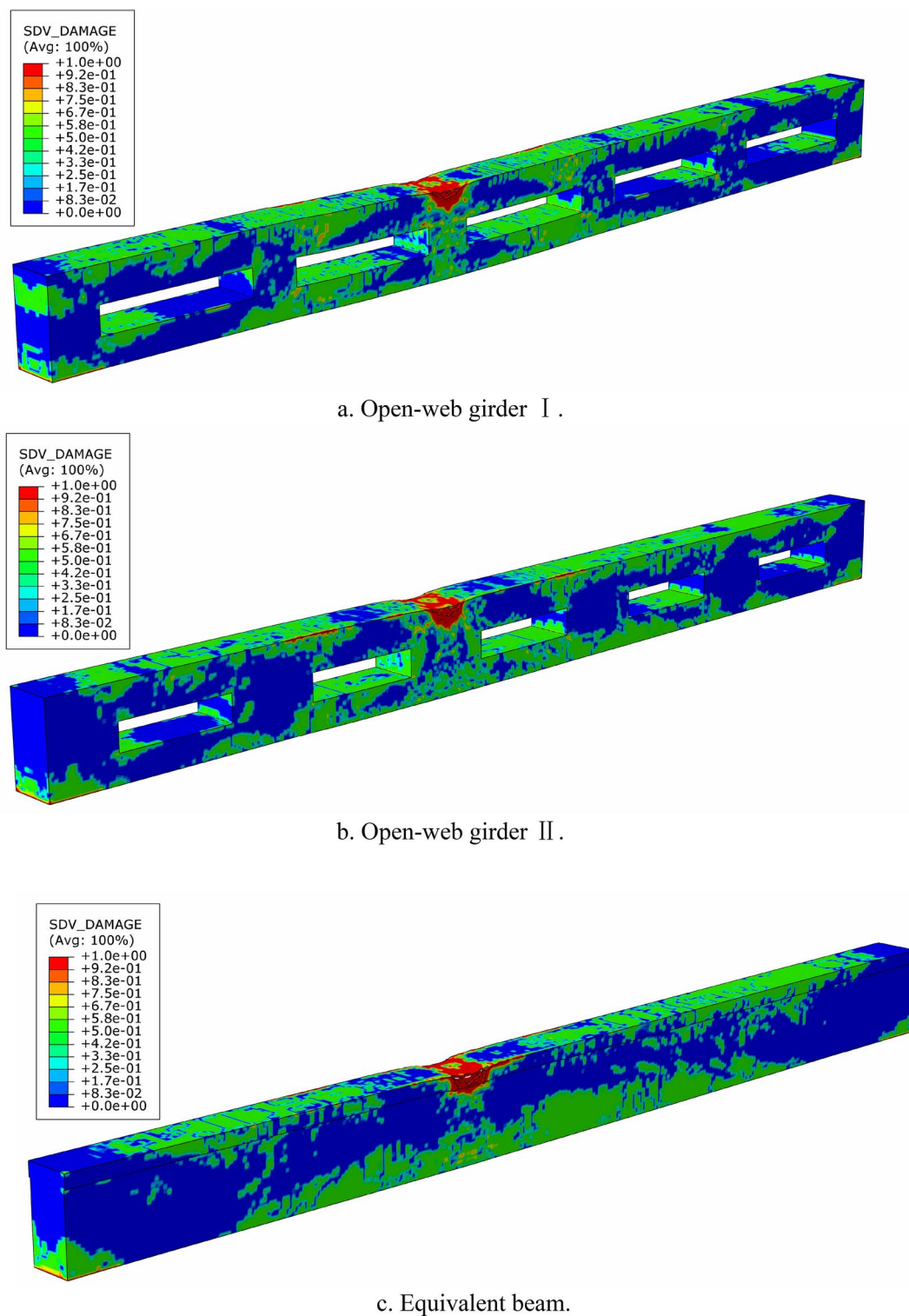
c. Equivalent beam.

Fig. 9. Damage results of concrete. (**a**) Open-web girder I. (**b**) Open-web girder II. (**c**) Equivalent beam.

II. In open-web girder I, significant damage is observed on both sides of the shear key closest to the explosion center point, accompanied by a noticeable increase in vertical displacement. The structure also displays evident bending and shear failure in terms of damage morphology, with localized shear failure marks present on the upper and bottom ribs. Overall, the damage level of open-web girder I is relatively severe, followed by open-web girder II, while the damage level of the Equivalent beam is the least severe. These results serve as a solid foundation for further analysis and discussion.

Displacement analysis

To visually observe the vertical displacement of the three structures, this study analyzed the vertical displacement data of the bottom rib points of the structures at two time points: 25 ms and 40 ms. Figure 10 demonstrates that during the numerical simulation, open-web girder I exhibited the largest vertical displacement, followed by open-web girder II, and finally Equivalent beam with the smallest displacement. The maximum displacement for all three structures occurred at the bottom of the structure closest to the center of the explosion.

At 25 ms, the maximum vertical displacement for open-web girder I, open-web girder II, and Equivalent beam were 56.4, 39.1, and 30.9 mm, respectively, with a maximum difference of 25.5 mm or 45.2%. At 40 ms, the maximum vertical displacement for open-web girder I, open-web girder II, and Equivalent beam were 54.2, 28.7, and 19.3 mm, respectively. The maximum difference between them was 34.9 mm, indicating a difference of 64.4%. According to the figure, the displacement response of the open-web girder is greatly influenced by the width of the shear key when subjected to explosive load. This suggests that increasing the width of the shear key can effectively reduce the displacement response of the structure. Comparing it with the Equivalent beam, both show similar trends in displacement response, but there are notable differences in the values. The author speculates that the open-web girder not only exhibits vertical displacement caused by the bending and shear deformation of solid-web girder but also the vertical displacement caused by local bending moments on the top and lower ribs, which is the main reason for the difference.

To better analyze the displacement patterns, we extracted displacement time history curves for three iconic positions (I, II, and III) of three different structures in Figs. 7, 8, respectively. Figure 11 illustrates the displacement time history curves for these three selected points. Overall, open-web girder I exhibits the highest maximum displacement, followed by open-web girder II, and the Equivalent beam shows the lowest maximum displacement. The vertical displacement trends of these three structures are generally similar, but there is a slight delay in the occurrence of maximum displacement for open-web girder I and open-web girder II compared to the Equivalent beam. This delay can be attributed to the separate stress characteristics of the upper and bottom ribs of the beam.

In Fig. 11-I the maximum displacement difference between the open-web girder I and the Equivalent beam is 26.4 mm, which accounts for 46% of the displacement. In Fig. 11-II the maximum displacement difference between the two is 27.7 mm, representing a difference of 48.4%. In Fig. 11-III the maximum displacement difference between the two is 11.2 mm, indicating a difference of 34.5%. These results highlight that while the open-web girder shares bending and shear characteristics with solid-web girders, the disparity between them should not be overlooked.

To deeply examine the impact of this variation on the structure, we extracted the horizontal displacement data of the cross-section plane at three positions (I, II, III) of three structures. This allowed us to analyze the torsion angle of the structure in the Z-axis direction and the alterations in the neutral axis position after structural damage. Figure 12 shows the horizontal displacement diagram of open-web girder I, with point I located at the geometric center of the shear key. Notably, the figure reveals substantial disparities in horizontal displacement at different points within the cross-section, indicating similarities to short columns experiencing shear and bending deformation. On the plane section at point II, the horizontal displacement of the top rib and concrete slab section conforms to the assumption of the section plane. However, the neutral axis position is not obvious, while the bottom rib section does not fully meet the assumption of the section plane. There is a significant horizontal slip between the top rib and the bottom rib. On the plane section at point III, the
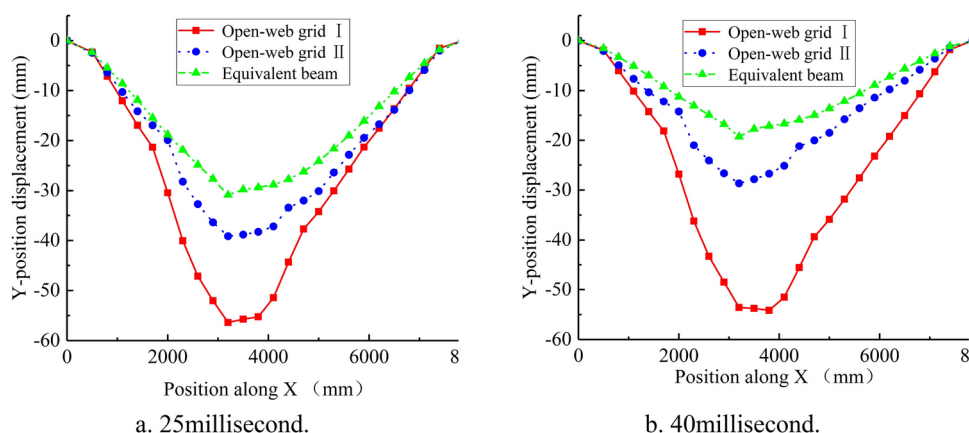

a. 25millisecond.   b. 40millisecond.

Fig. 10. Vertical displacement of structures at different times. (**a**) 25ms. (**b**) 40ms.

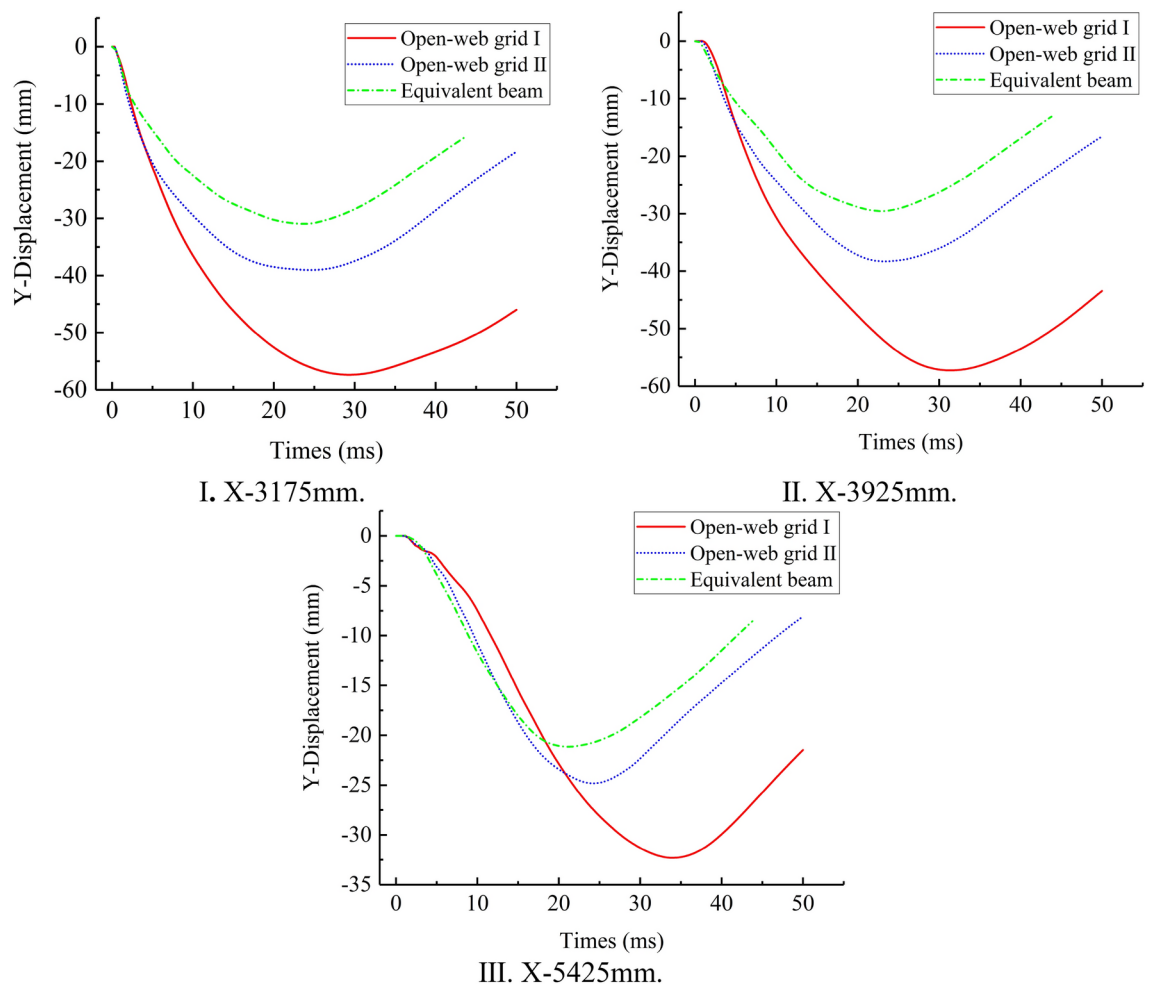I. X-3175mm.

II. X-3925mm.

III. X-5425mm.

Fig. 11. Vertical displacement of structures at different positions.

deformation of the top rib conforms to the assumption of the section plane, with the neutral axis position visible, and the deformation of the bottom rib also basically conforms to the assumption of the section plane. Although the neutral axis position is not obvious, there is still a significant sliding phenomenon between the top rib and the bottom rib.

Figure 13 shows the horizontal displacement diagram of open-web girder II, the displacement of the upper points in the plane section of point I is relatively discrete, which is due to severe concrete damage here. The displacement of the bottom rib points conforms to the assumption of the plane section, and it can be preliminarily observed that the neutral layer is located at the position of the bottom rib, with no significant slip between the top and bottom ribs. The displacement of each point on the plane section of the top rib at point II conforms to the assumption of the plane section, but the displacement of the bottom rib points of the section does not fully conform to the assumption of the plane section, and there is a significant slip between the top and bottom ribs. In the plane section at point III, the displacement of each point conforms to the assumption of the plane section, but there is a slight slip between the top and bottom ribs, and the neutral layer is located at the position of the top rib. By comparing Figs. 12, 13, it can be found that increasing the width of the shear key can effectively reduce the shear deformation of the shear key, making the deformation of the overall open-web girder more inclined towards the stress characteristics of the solid-web girder. Compared with Fig. 13-I and Fig. 13-III it is shown that the neutral layer of the section near the damaged area of the structure under impact load has shifted downwards, located at the position of the bottom rib. At the same time, compared with Fig. 13-II and Fig. 13-III, the comparison shows that the slip of the top and bottom ribs is more obvious in the severely damaged area of the structure and is more affected by local bending moments.

Figure 14 shows the horizontal displacement diagram of the Equivalent beam, through a comprehensive comparison and analysis of the horizontal displacement curves of the flat sections in Figs. 12, 13, 14, it can be further confirmed that the width of the shear key significantly influences the displacement response of the open-web girder under explosive loads. When the shear key is narrow, the top ribs, bottom ribs, and shear keys in the open-web girder experience substantial bending moments and shear forces. This is evident in the significant slip between the top and bottom ribs, resulting in a much larger vertical displacement of the open-web girder structure compared to the solid-web girder. However, as the width of the shear key increases, the local bending
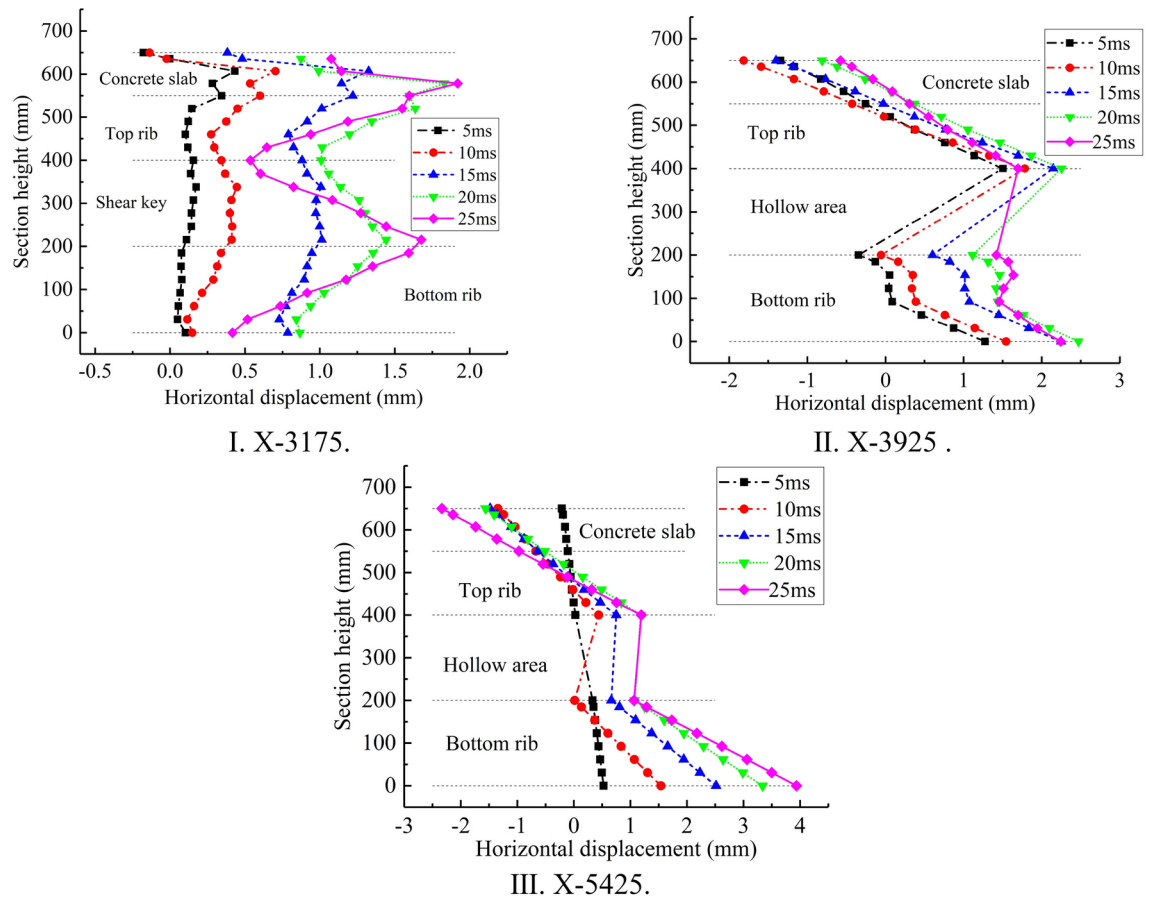
Fig. 12. Horizontal displacement curve of open-web girder I.

moments of the top rib, bottom rib, and shear key gradually decrease, leading to a corresponding reduction in vertical displacement difference. Consequently, the stress characteristics of the open-web girder gradually align with the response observed in the solid-web girder.

Stress analysis

To analyze the stress situation of the top and bottom ribs, the horizontal stress components of the steel bars on sections I, II, and III of the open-web girder I, open-web girder II, and Equivalent beam were extracted (the steel bars were positive in tension and negative in compression). For example, a-2 represents the reinforcement at the intersection of horizontal axis a and vertical axis 2 in Fig. 8, similar to others.

As shown in Figs. 15, 16, 17, a-2 represents the lower reinforcement of the bottom rib, b-2 represents the upper reinforcement of the bottom rib, c-2 represents the lower reinforcement of the top rib, and d-2 represents the upper reinforcement of the top rib. In Fig. 15-I, reinforcement a-2 is in a tensile state throughout the entire process, with a maximum tensile stress of 434 MPa; The steel bar b-2 is under compression during the 0–14 ms, with a maximum compressive stress of 428 MPa. During the period of 14–50 ms, the steel bars experienced a tensile state with a maximum tensile stress of 140 MPa. In Fig. 17-I both reinforcement a-2 and b-2 are subjected to tension throughout the entire process, with a maximum tensile stress of 428 MPa. These results indicate that under the action of explosive impact load, the bottom rib on the cross-section I of open-web girder I first exhibit the characteristics of a beam, bearing bending moments, causing the lower reinforcement of the bottom rib to be tensioned and the upper reinforcement of the bottom rib to be compressed.

As the vertical displacement of the structure increases, the local bending moment on the bottom rib gradually decreases, and the upper reinforcement of the bottom rib gradually begins to be tensioned, with a maximum tensile stress of 140 MPa, which is 32.3% of the maximum tensile stress of the lower reinforcement of the bottom rib. In Fig. 15-I, the steel bars c-2 and d-2 are in a tensile stress state throughout the entire process, with maximum tensile stresses of 428 MPa and 406 MPa, respectively. However, there is a significant difference in the stress characteristics of steel bars c-2 and d-2 compared to Fig. 17-I. In Fig. 17-I, reinforcement c-2 first experiences tensile stress, with a maximum value of 308 MPa; Subsequently, the tensile stress rapidly decreased and remained below 80 MPa until the end of the simulation. On the contrary, reinforcement d-2 first bears compressive stress, with a maximum value of 429 MPa; Subsequently, it rapidly transformed into tensile stress, with a maximum value of 426 MPa, and continued to be subjected to compressive stress until the end of the simulation.
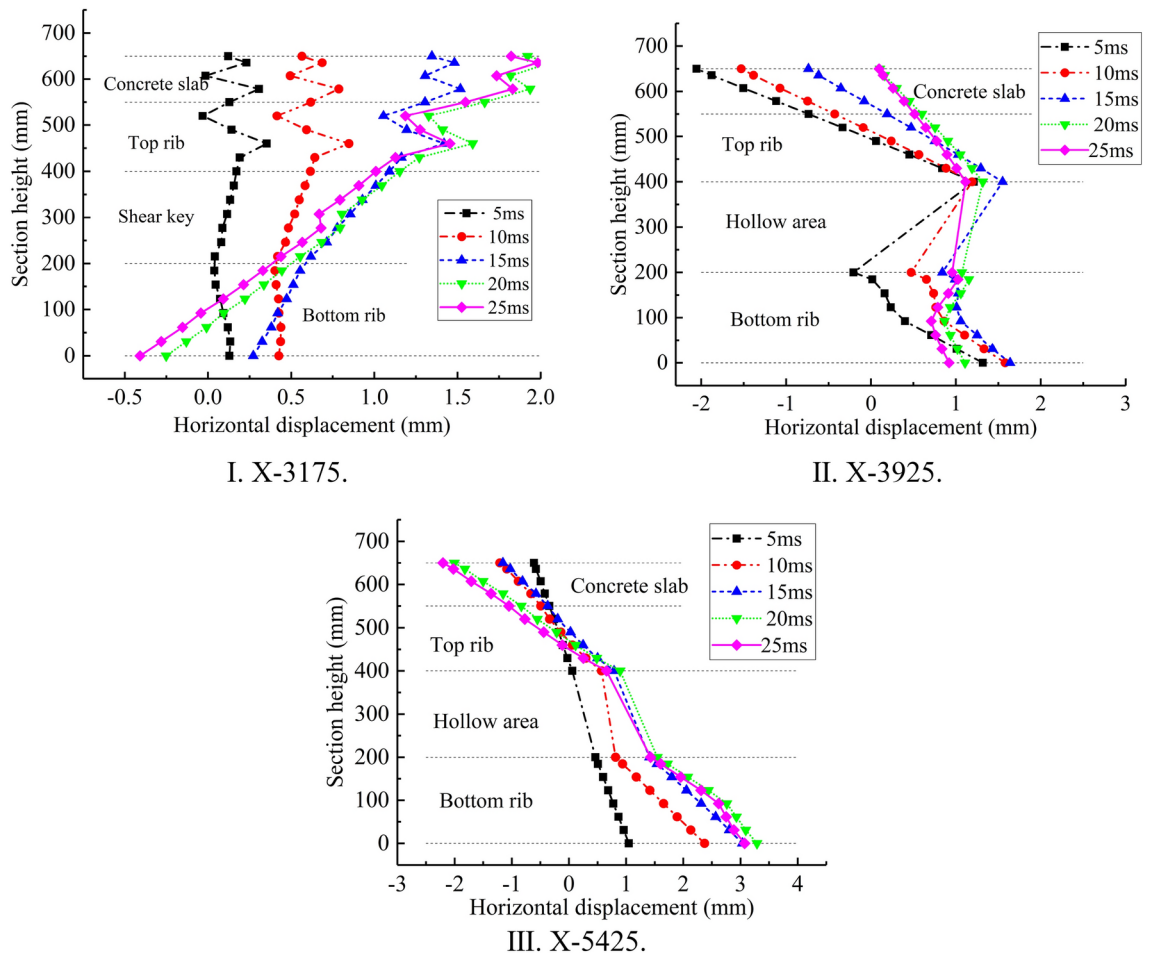
I. X-3175.

II. X-3925.

III. X-5425.

Fig. 13. Horizontal displacement curve of open-web girder II.

After the above analysis, it can be observed that in the open-web girder I structure, there is a significant difference in the overall trend of the stress on the steel bars at the section position (X = 3175) compared to the stress trend on the steel bars at the same section position in the equivalent beam. In the process of explosion simulation, the open-web girder I is mainly subjected to tensile force by the a-2 steel bars, while the equivalent beam structure is jointly subjected to tensile force by the a-2 and b-2 steel bars. When the explosion wave acts on the initial section I of the open-web girder I, b-2 bears pressure, but then quickly releases. In equivalent beam structures, d-2 steel bars are mainly subjected to pressure. In general, in the case of narrow shear keys, there is a noticeable difference in the stress state of the steel bars in the open-web girder structure compared to the solid-web girder. Specifically, the steel bars in the upper of the top ribs and lower layers of the bottom ribs experience higher levels of stress in the open-web girder structure. However, as the width of the shear keys increases, the stress characteristics of the steel bars gradually approach those of the solid-web girder structure.

Conclusions

This study conducted a simulation of the explosion test described in the literature and compared the numerical simulation results with experimental data. The results demonstrated a strong consistency between the two, confirming the reliability of the numerical simulation method and material constitutive parameters utilized. Subsequently, the same method was used to analyze the dynamic response of three structures under an explosion load equivalent to a scaled distance of 0.5 m /kg$^{1/3}$, leading to the following conclusions:

Under the same explosive load, both the open-web girder and the solid-web girder show similar damage. However, the connection points of the top ribs, bottom ribs, and shear keys of the open-web girder are more vulnerable to impact loads. In particular, the tensile area of the bottom rib may develop premature tensile fracture cracks. Furthermore, the main failure mode of the structure is the tensile failure of the bottom ribs of the open-web girder.

The overall characteristics of vertical displacement between open-web girders and solid-web girders are similar. In general, solid-web girders experience smaller vertical displacements compared to open-web girders when subjected to equivalent treatment. By increasing the width of the shear key, it is possible to effectively reduce the vertical displacement of the structure without the additional structural reinforcement. When calculating the vertical displacement of an open-web girder, it is recommended to consider two components: the
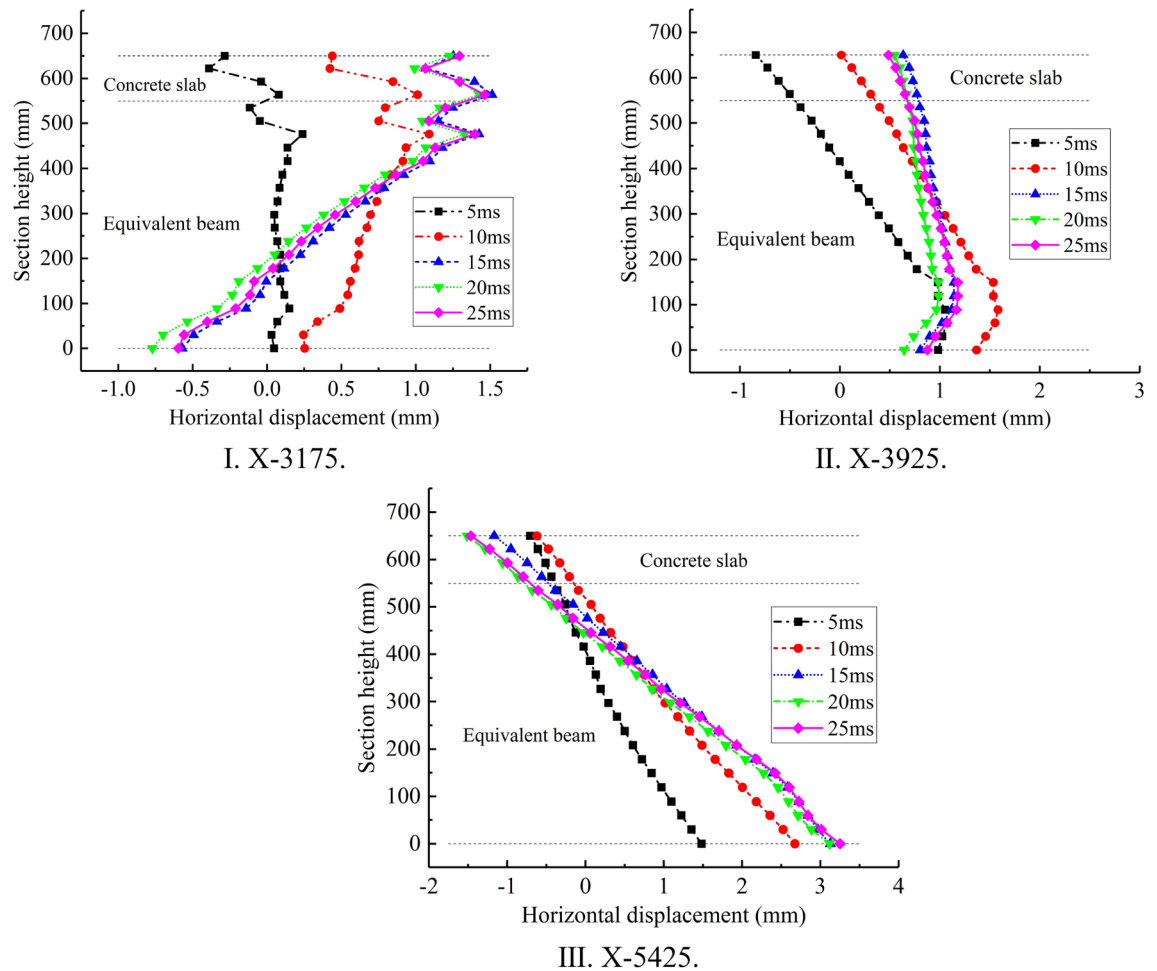
Fig. 14. Horizontal displacement curve of Equivalent beam.

overall bending deformation and the deformation caused by the local bending moment of the top ribs, bottom ribs, and shear key.

When designing narrow shear keys, the top ribs, bottom ribs, and shear keys of the open-web girders will exhibit significant bending and shear deformation, and there may be significant slippage between the top and bottom ribs. Based on this, in practical engineering, shear keys with sufficient width should be designed.

The tensile stress in the lower layer of the bottom ribs is significantly higher than that in the upper layer. Similarly, the compressive stress in the upper layer of the top ribs is significantly higher than that in the lower layer. Therefore, In the design of structural reinforcement, it is recommended to arrange a maximum number of steel bars in the upper part of the top ribs and the lower layers of the bottom ribs. This arrangement aims to optimize the performance of the steel bars. The ultimate bearing capacity of the structure is reached when the steel bars in the lower layer of the bottom ribs reach their yield strength. Hence, it is important to consider appropriate safety reserves when calculating the reinforcement of the lower layer of the ribs. Additionally, it is important to place structural bars at the connection points between the shear key and the upper and bottom ribs. This helps to resist local bending moments at the nodes and prevent premature failure.
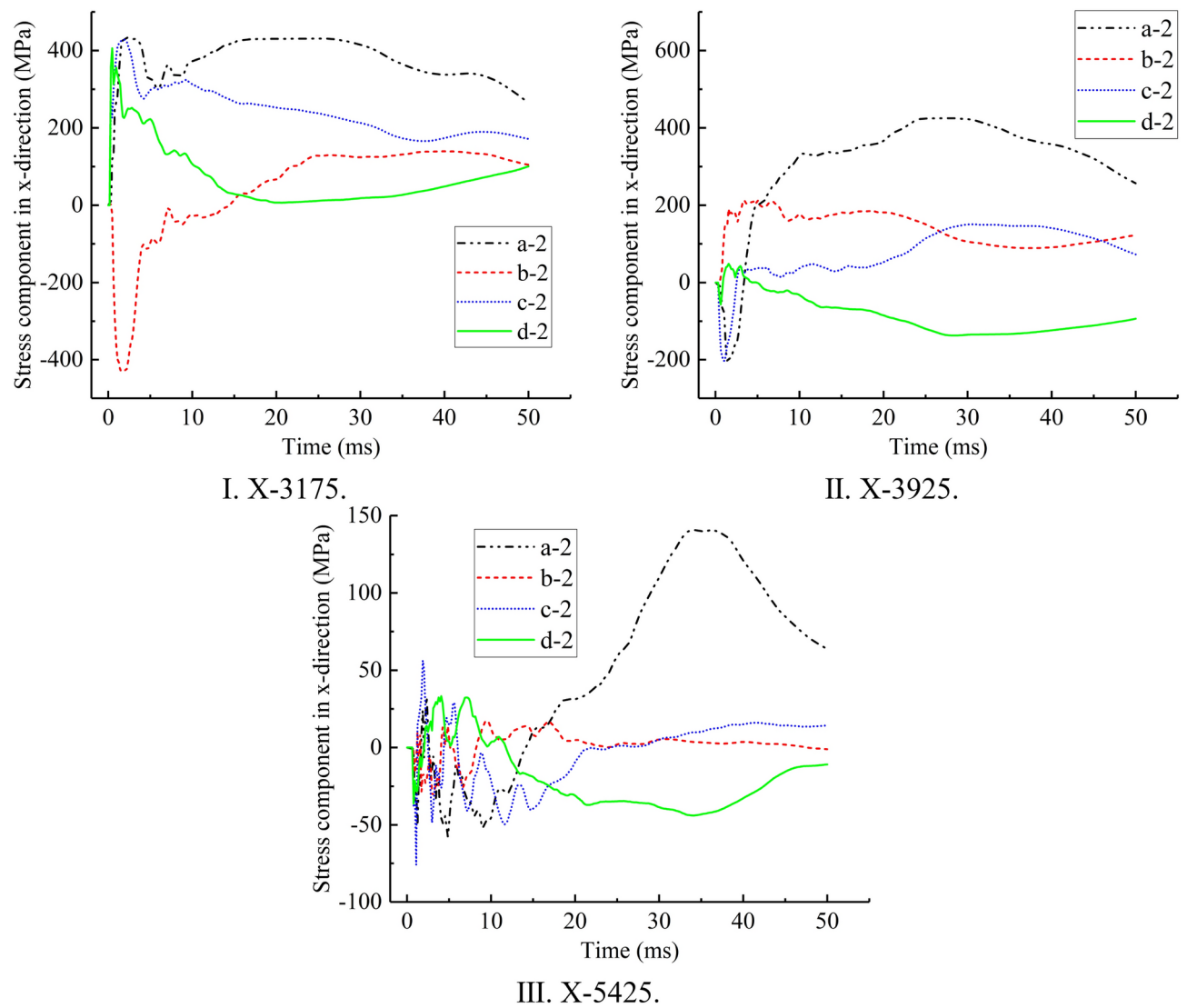
I. X-3175.

II. X-3925.

III. X-5425.

Fig. 15. Stress time history curve of open-web girder I.

I. X-3175.

II. X-3925.

III. X-5425.

Fig. 16. Stress time history curve of open-web girder II.
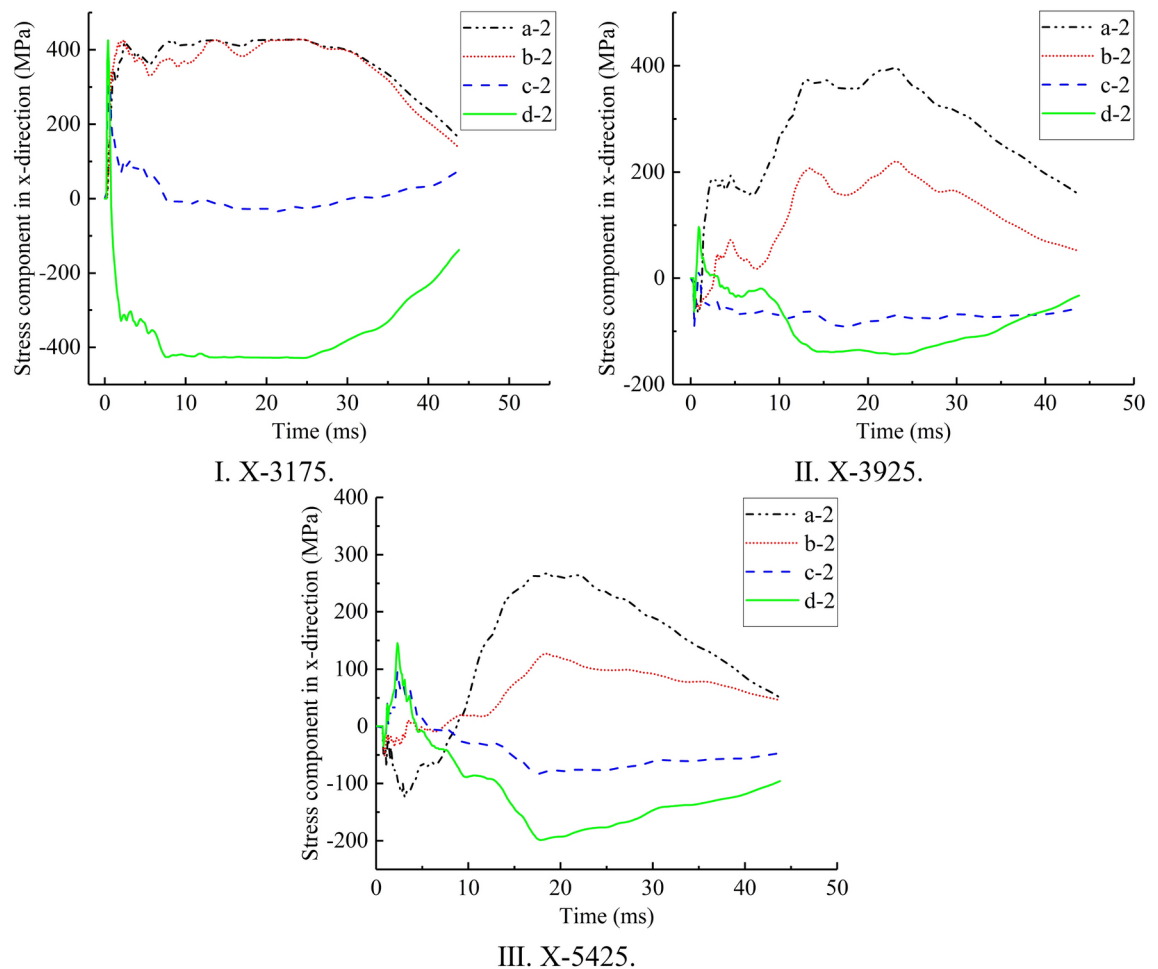
I. X-3175.

II. X-3925.

III. X-5425.
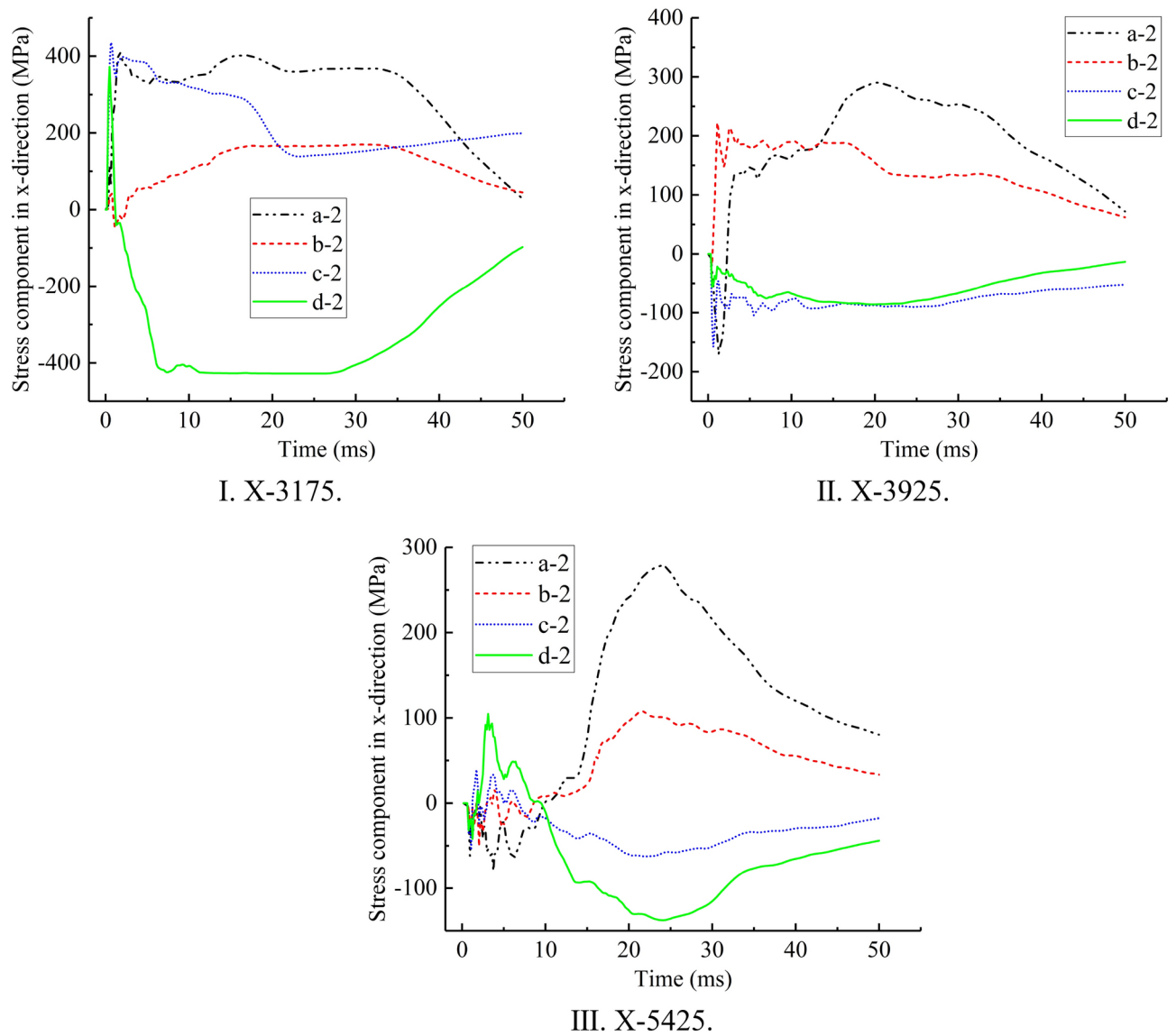
Fig. 17. Stress time history curve of Equivalent beam.

Data availability
Data is provided within the manuscript or supplementary information files.

References
1. Kejian, M. A. et al. *Theory and Practice of New Type Architecture Space Griding Structures* (China Communications Press, 2006).
2. Shilin, D. O. N. G. The development history, innovation, classification, and practical application of spatial structures. *Spat. Struct.* **1**, 522–43 (2009).
3. Dingyuan, L. I. U. et al. Bending theory of Vierendeel sandwich plate based on variational method. *Compos. Struct.* **30** (9), 6116570 (2023).
4. Fang, Y. U. et al. Experimental study of a new assembled integral concrete-steel open-web sandwich plate composite bridge. *Eng. Struct.* **27**, 2115018 (2022).
5. Kejian, M. A. et al. Study and application of long span reinforced concrete vierendeel sandwich plate. *J. Build. Struct.* **2**, 116–23 (2000).
6. Lan, J. I. A. N. G. et al. Human-induced-vibration response analysis and comfort evaluation method of large-span steel vierendeel sandwich plate. *Buildings* **12**, 1228 (2022).
7. Duodong, W. U. et al. Analysis and design of large-span concrete open-web sandwich slab floor. *Build. Struct.* **4**, 81–6 (2018).
8. Tong, X. I. A. O. et al. Dynamic characteristics and seismic performance analysis of new high-rise fabricated steel grid box structure. *J. North China Univ. Sci. Technol. (Nat. Sci. Ed.)* **44**, 60–7 (2022).
9. Space Structures Research Center of Guizhou University. Technical specification for reinforced concrete open-web sandwich plate structures(S). DB22/48–2005[S]. (2005).
10. Jin, S. O. N. & Lee, Ho-Jung. Performance of cable-stayed bridge pylons subjected to blast loading. *Eng. Struct.* **33**, 1133–48 (2011).
11. Yanchao, S. H. I. et al. A new method for progressive collapse analysis of RC frames under blast loading. *Eng. Struct.* **32**, 1691–703 (2010).
12. Jing, W. A. N. G. *Experimental and Numerical Studies on the Local Damage of Reinforced Concrete Slabs under Close-in Explosions* (Tianjin university, 2016).
13. Jun, L. I. et al. Investigation of ultra-high performance concrete slab and normal strength concrete slab under contact explosion. *Eng. Struct.* **102**, 395–408 (2015).

14. Vaishnavi, J. K. & Krishna, B. M. Determination of response of multistorey structure subjected to blast loading. *J. Build. Pathol. Rehabil.* https://doi.org/10.1007/s41024-022-00218-6 (2022).
15. Bo, Y. A. N. et al. Numerical study on damage mechanism of RC beams under close-in blast loading. *Eng. Fail. Anal.* **51**, 9–19 (2015).
16. Rajkumar, D. et al. Numerical study on parametric analysis of reinforced concrete column under blast loading. *J. Perform. Construct. Facil.* https://doi.org/10.1061/(ASCE)CF.1943-5509.0001382 (2020).
17. Sherong, Z. H. A. N. G. et al. Numerical simulation of failure modes of concrete gravity dams subjected to underwater explosion. *Eng. Fail. Anal.* **3**, 649–64 (2014).
18. Oucif, C. & Mauludin, L. M. Numerical modeling of high velocity impact applied to reinforced concrete panel. *Undergr. Space* **4**, 1–9 (2019).
19. Jie, L. U. O. et al. Dynamic response analysis on steel Vierendeel sandwich plate structures under explosive loading. *Spat. Struct.* **2**, 456–61 (2018).
20. Xiaohua, Z. H. A. O. & Gaohui, W. A. N. G. Damage features of RC slabs subjected to air and underwater contact explosions. *Ocean Eng.* **147**, 531–45 (2018).
21. Jun, L. I. et al. Investigation of ultra-high performance concrete slab and normal strength concrete slab under contact explosion. *Eng. Struct.* **10**, 2395–408 (2015).
22. Yifei, H. A. O. et al. Numerical analysis of lateral inertial confinement effects on impact test of concrete compressive material properties. *Int. J. Protect. Struct.* **1**, 145–67 (2010).
23. Hao, Y. F. et al. Numerical analysis of concrete material properties at high strain rate under direct tension. *Procedia Eng.* **14**, 336–43 (2011).
24. Gordon, R. & Johnson, T. J. H. An improved computational constitutive model for brittle materials. *High Press. Sci. Technol.* **309**, 981–984 (1993).
25. Ping, X. U. & Sixian, Z. U. O. Study on the JH-2 Model Parameters for Metro Shield Cutting Reinforced Concrete Pile. *Geotech. Geol. Eng.* **395**, 267–78 (2021).
26. Codina, R. et al. Experimental and numerical study of an RC member under a close-in blast loading. *Eng. Struct.* **127**, 145–58 (2016).
27. Johnson, G. R. & Cook, W. H. Fracture characteristics of three metals subjected to various strains, strain rates, temperatures and pressures. *Eng. Fract. Mech.* **21**(1), 31–48 (1985).
28. Yukai, W. A. N. G. & Jianxin, Z. H. A. O. Tensile fracture test and numerical simulation of Q235 steel. *J. Plast. Eng.* **26**(1), 168–73 (2019).
29. Lee, E. L. & Tarver, C. M. Phenomenological model of shock initiation in heterogeneous explosives. *Phys. Fluids* **23**, 2362 (1980).
30. AUTODYN. Theory Manual. Century Dynamic. (2006).
31. SIMULIA User Assistance 2022. Dassault Systems SIMULIA Corp. (2022).

Author contributions
Zongyuan Fan and Kaicong Kuang conceived of the presented idea and directed the project. Zongyuan Fan planned and carried out the computational modeling and simulations. Yanhui Wei and Jing Chen developed the theoretical framework. Zongyuan Fan wrote the manuscript with input from all authors. Kejian Ma,Jing Chen ,Penggang Tian and Bingzhen Zhao helped supervise the project. Zongyuan Fan, Yanhui Wei drafted the manuscript and designed the figures. All authors discussed the results and contributed to the final manuscript. All authors reviewed the manuscript.

Declarations

Competing interests
The authors declare no competing interests.

Additional information
Correspondence and requests for materials should be addressed to Y.W.

Reprints and permissions information is available at www.nature.com/reprints.

Publisher's note Springer Nature remains neutral with regard to jurisdictional claims in published maps and institutional affiliations.